Supplementary Materials for

Inter-crystallite Bragg Scattering Decodes the Nanostructure of Hard Carbon for Sodium Storage and Beyond

Jianyuan Wu[1,2]*, Xinli Wang[1,2,3], Liekai Liu[4], Yongcheng Zou[4], Lai-An Tan[5], Wen-Chun Yen[4,5], Ang Li[6], Juping Xu[1,2], Yuanguang Xia[1,2], Huaican Chen[1,2], Wen Yin[1,2], Zu-Wei Yin[7], Wenhai Ji[1,2], Nan Zheng[8], Hua Yang[1,2], Guang Wang[1,2], Jian Zhu[9], Yiping Zhang[9], Enyue Zhao[10], Takashi Kamiyama[1,2], Fangwei Wang[1,11], Wang Hay Kan[1,2]*

*Corresponding authors: jywu@ihep.ac.cn (J.W.); jianhx@ihep.ac.cn (W.H.K.)

Contents

Supplementary Text

Text S1. General characterisation and electrochemical testing of KC15

The elemental composition of KC15 was determined as 98.88% carbon, 0.28% hydrogen, 0.72% oxygen, and 0.12% nitrogen, indicating a high purity of KC15. At the microscale, SEM revealed an average particle size of approximately 10 μm (Extended Data Fig. 1a). BET analysis confirmed the absence of open pores (Extended Data Fig. 1b). At the mesoscale, SAXS indicated the presence of closed pores with a diameter of 3.4 nm (Extended Data Fig. 1c). A crystallite (grain) size was determined to be 5.86 nm, calculated using an empirical equation [51] with Raman spectra data (Extended Data Fig. 1d). At the atomic scale, the XAS peak (Extended Data Fig. 1e) at 286.0 eV indicates a hexagonal ring structure [66, 67]. Furthermore, the peak at 287.8 eV suggests that some of these ring-based layers form interlayer stacking [67, 68]. The pre-edge peak at 282.2 eV is attributed to the states at the graphene edge [69]. The peaks at 287.2 eV and 288.7 eV are related to carbon-oxygen bonds [68, 70, 71], which probably results from ambient adsorption on the surface. The projections of both parallel stacking and random distributed layers were observed on the TEM image (Extended Data Fig. 1f). The X-ray diffraction (XRD) patterns (Extended Data Fig. 1g) exhibited typical patterns of hard carbon [10], which comprise three broad peaks and a rising pattern in the low-angle region.

KC15 performed a reversible capacity of 320.8 $mAh\,g^{-1}$ and a coulombic efficiency of 87.6% during the first electrochemical cycle. The voltage–capacity profile exhibited typical characteristic of hard carbon [4, 5], including a sloping stage and a plateau stage (Extended Data Fig. 2).

Text S2. Diffraction contribution from intra- and inter-crystallite Bragg order: a theoretical derivation

The diffraction intensity of specific crystallographic plane (h k l) from per unit volume of crystallite can be expressed by the following formula:

$$I = N_{\mathrm{c}} N_{\mathrm{p}}^2 I_{\mathrm{p}}$$

where, N_{c} is the number of crystallites per unit volume, N_{p} is the number of specific crystallographic plane in a crystallite, and I_{p} denotes the diffraction intensity contributed by a single crystallographic plane.

For the sake of our analysis, we consider a crystallite in the form of a cube with an edge length L, representing the crystallite size. Thus, the area of a crystallographic plane is given by L^2 and the volume of a single crystallite is given by L^3, yielding

$$N_{\mathrm{c}} = \frac{1}{L^3}$$

Assuming the interplanar distance is denoted by d, the number of specific crystallographic planes within a cubic crystallite is given by

$$N_{\mathrm{p}} = \frac{L}{d}$$

For the RPP model, we simplify this by assuming there is only one crystallographic plane per crystallite, thus

$$N_{\mathrm{p}} = 1$$

According to the Thomson equation [30], the absolute intensity of the X-ray wave coherently scattered by a single electron, I_{e}, is expressed as

$$I_e = I_i \frac{K}{r^2} \left(\frac{1 + cos^2 2\theta}{2}\right)$$

where, I_{i} is the absolute intensity of the incident beam, K is constant (K = 7.94×10−30 m^2), r is the distance from the electron to the detector in m, and θ is the Bragg angle. It is noteworthy that in a powder XRD experiment with identical instrumental parameters, all prefactors in the right hand side of the Thomson equation are constant, with the only variable being a function of the Bragg angle. Let I_0 represent the absolute coherently scattered intensity contributed by a unit area of the crystallographic plane, which remains constant when the atomic type, the density of atoms within the plane, and instrumental parameters of diffraction experimental are setup. The equation can be expressed as

$$I_e = I_o \left(\frac{1 + cos^2 2\theta}{2}\right)$$

Consequently, the intensity contributed by a single crystallographic plane, I_{p}, can be expressed as

$$I_p = I_e \cdot L^2 = I_o L^2 \left(\frac{1 + cos^2 2\theta}{2}\right)$$

As a result, for specific crystallographic planes within crystallites, i.e. the intra-crystallite condition, the diffraction intensity from per unit volume can be formulated as

$$I_{\mathrm{intra}} = \frac{1}{L^3} \cdot \left(\frac{L}{d}\right)^2 \cdot I_0 \cdot L^2 \left(\frac{1 + cos^2 2\theta}{2}\right) = \frac{I_0 L}{d^2} \left(\frac{1 + cos^2 2\theta}{2}\right)$$

According to the Bragg's law [32],

$$d = \frac{\lambda}{2sin\theta}$$

where, λ is the wavelength. Substituting into the preceding equation, we obtain

$$I_{\text{intra}} = \frac{2I_0 L sin^2\theta(1 + cos^2 2\theta)}{\lambda^2}$$

In the context of the RPP model, for the specific crystallographic planes across crystallites, i.e. the inter-crystallite condition, the diffraction intensity from per unit volume can be formulated as

$$I_{\text{inter}} = \frac{1}{L^3} \cdot (1)^2 \cdot I_0 \cdot L^2 (\frac{1 + cos^2 2\theta}{2}) = \frac{I_0(1 + cos^2 2\theta)}{2L}$$

By omitting the absolute intensity I_0, we define the relative intensities as

$$I'_{\text{intra}} = \frac{2L sin^2\theta(1 + cos^2 2\theta)}{\lambda^2}$$

and

$$I'_{\text{inter}} = \frac{(1 + cos^2 2\theta)}{2L}$$

Next, we define a ratio R between I'_{intra} and I'_{inter}. A smaller R indicates a more pronounced I'_{inter}.

$$R = \frac{I_{\text{intra}}}{I_{\text{inter}}} = \frac{4L^2 sin^2\theta}{\lambda^2} = \frac{L^2}{d^2}$$

This ratio R is proportional to the square of the crystallite size. Consequently, smaller crystallite sizes lead to a decreased R, which correlates with a more pronounced diffraction intensity from the inter-crystallite condition. Conversely, R is inversely proportional to the square of interplanar distance, indicating that the signal from inter-crystallite diffraction becomes more prominent in regions of low d-spacing (low Bragg angle region).

For instance, when λ is set to 1.54 Å, we illustrated the plots of I'_{intra} and I'_{inter} as a function of crystallite size at the Bragg angle $2\theta = 10^{\circ}$ (Fig. 2b). When the crystallite size falls below 8 nm, the ratio R drops below the order of 10^1, indicating a significant enhancement in the observability of inter-crystallite diffraction signal. Additionally, we present the plots of I'_{intra} and I'_{inter} as a function of Bragg angle across various crystallite sizes (Supplementary Fig. S5). At a crystallite size of 1 nm, the contribution from inter-crystallite diffraction even surpasses that from intra-crystallite diffraction in the low Bragg angle region. As the crystallite size decreases, the range of Bragg angles affected by this nano-effect broadens.

On the other hand, as the crystallite size increases to several tens of nanometres and beyond, the ratio R rises to 10^3 and larger, suggesting that the inter-crystallite contribution becomes too small to be detected. This returns us to a regime where the classical theories can be effectively applied.

Additionally, for neutron scattering, the intensity contributed by a single crystallographic plane, I_p, can be expressed as

$$I_p = I_n \cdot L^2 = b^2 L^2$$

where, I_n is the absolute intensity of the neutron wave coherently scattered by an atom, b the neutron scattering length of specific element. Thus, for the intra-crystallite condition, the neutron diffraction intensity from per unit volume can be formulated as

$$I_{\text{intra}} = \frac{1}{L^3} \cdot \left(\frac{L}{d}\right)^2 \cdot b^2 \cdot L^2 = \frac{b^2 L}{d^2}$$

and for the inter-crystallite condition, the neutron diffraction intensity from per unit volume can be formulated as

$$I_{\text{inter}} = \frac{1}{L^3} \cdot (1)^2 \cdot b^2 \cdot L^2 = \frac{b^2}{L}$$

Since the scattering length b is identical for atoms of the same element, the absolute scattering length is omitted, and the relative intensities are defined as

$$I'_{\mathrm{intra}} = \frac{L}{d^2}$$

and

$$I'_{\mathrm{inter}} = \frac{1}{L}$$

Accordingly, the ratio R,

$$R = \frac{I_{\mathrm{intra}}}{I_{\mathrm{inter}}} = \frac{b^2 L}{d^2} \cdot \frac{L}{b^2} = \frac{L^2}{d^2}$$

Here, the R in ND is identical to the condition in XRD.

We also illustrated the plots of I'_{intra} and I'_{inter} as a function of crystallite size under the ND conditions (Supplementary Fig. S6), which exhibits trends similar to those observed in XRD.

Text S3. Critical distance for forming a RPP condition: a theoretical estimation

We considered two randomly parallel planes, with the condition that the angle between their normals is limited to less than 1°[15]. There are 360^3 possible configurations that satisfy this condition. To achieve the RPP condition for each plan, we require a double amount of planes. As assumed upon, there is only one crystallographic plane per crystallite. The total volume of crystallites is

$$V_c = 2 \cdot 360^3 \cdot L^3$$

When these crystallites randomly distribute in a sphere, the average interplanar distance of a RPP cell corresponds to the radius of the sphere, r. By equating volumes, we have

$$V_c = V_{sphere} = (4/3)\pi r^3$$

From this, we can derive

$$r = \left(\frac{3}{2\pi}\right)^{\frac{1}{3}} \cdot 360 \cdot L \approx 280L$$

This implies that a plane can find its parallel partner on average at a distance of approximately 280 times its crystallite size. For nanomaterials, this distance falls within the interaction region of the incident beam [30].

Text S4. Structural prediction of the sodiated phases

The four phases of KC15 were adopted as hosts for the corresponding sodiated phases. The peak positions of KC15 observed in the *in situ* ND remained largely unchanged throughout the discharge/charge process (Fig. 3a, c), indicating stable lattice constants during the sodiation/desodiation processes. This stability enables the construction of sodiated structures using the refined structural parameters of KC15 (Supplementary Table S2).

Considering the reported capacities [4, 5] and relevant analyses of hard carbon samples in previous studies [41], we assumed that intercalation models (sodium atoms were inserted into the center between two carbon layers) were applicable to the graphite phases with a fully sodiated concentration of NaC_6 (Supplementary Fig. S9-S11), while adsorption model (sodium atoms were adsorbed on carbon layers at a stable distance) was applied to the graphene phase with a concentration of NaC_3 (Supplementary Fig. S12). Expanded supercells for sodiated phases were constructed based on their respective host phases, with the expansion ratios depending on the respective fully sodiated concentrations (Supplementary Table S7).

Initially, sodium atoms were uniformly assigned to all possible sites corresponding to the centers or nodes of hexagonal carbon rings (Supplementary Fig. S9-12a, b, c). The occupancies of these sodium sites were evenly apportioned according to their fully sodiated concentrations. Based on these average models (Supplementary Fig. S9-12a, b, c), the actual atomic models (with one sodium atom per site) were calculated using the *Supercell* software [60]. All mathematically possible configurations and their relative energies were generated (Supplementary Fig. S9-12d). The lowest-energy configurations for each sodiated phase (Supplementary Fig. S9-12e, f, g) were selected for further simulation and calculation. Prior to simulating the diffraction patterns, DFT calculations were performed to determine the accurate stable positions of all atoms within the selected phases.

The configurations of NaC_{24} and NaC_{12} were also produced using the same process described above.

Text S5. Pattern offsetting of *in situ* ND for clearer observation and comparison

As sodiation progresses into the plateau electrochemical stage, the overall intensity of the measured TOF-ND patterns significantly increases (Fig. 3a, c), which interferes with the visibility of patterns attributed to other phases. Therefore, we used the peak of Al (1 1 1) from the Al current collector as a reference point, where no significant changes in the simulated patterns attributed to other phases occur during the sodiation process. We offset the obtained *in situ* TOF-ND patterns to align with the fixed peak height of Al (1 1 1) for clearer observation (Supplementary Fig. S13a, c). A similar offset was also applied to the simulated patterns of the graphene phase, which exhibit only slight changes during the sodiation process (Supplementary Fig. S13d). This operation facilitates a clearer examination of the *in situ* TOF-ND patterns and their comparison with the simulated patterns (Fig. 3d, f, h; Supplementary Fig. S13d).

The decreasing intensity of the broad peak around 3–5 Å throughout the entire sodiation process can be more readily observed (Supplementary Fig. S13a, c), which is attributed to intercalation behaviour within one or more of the three graphite phases (Fig. 3d, f, h).

The patterns of Na metal with varying grain sizes were simulated (Supplementary Fig. S13e). At the corresponding Bragg positions, sharper Na patterns are observed (Supplementary Fig. S13a, c), attributed to the Na metal from the counter electrode. These patterns decrease as Na electrode is consumed during the sodiation process of KC15 and reverse during the desodiation process (Supplementary Fig. S13a, c). Notably, no peaks as broad as those in the simulated patterns (Supplementary Fig. S13e) were present during the entire sodiation process, indicating that no Na metal or clusters smaller than 3 nm in diameter were formed during this process.

Text S6. *In situ* XRD studies for sodiation process

The *in situ* XRD study (Extended Data Fig. 9) was employed for cross-validation, which exhibited distinct pattern features compared to those observed in the ND. The *in situ* XRD patterns (Extended Data Fig. 9a, c) are similar to reported results [72, 73]. The sodiated phases used above (Fig. 3e, g, i, k) were also applied to simulate XRD patterns (Extended Data Fig. 9d-g). The broad peak around 14-30° decreases throughout the entire sodiation process (Extended Data Fig. 9a, c), matching well with the simulated patterns of the three sodiated graphite phases (Extended Data Fig. 9d-f), which indicates intercalation processes within these three phases or a few of them. The sloping pattern around 10–15° significantly declines as the sodiation progresses into the plateau stage, aligning well with the changes in the simulated patterns (Extended Data Fig. 9g), which indicates a sodium adsorption within the graphene phase. The pattern emerging from around 24°-34° (Extended Data Fig. 9a, c) should result from both intercalation (Extended Data Fig. 9d-f) and adsorption (Extended Data Fig. 9g) behaviours.

In some studies, this emerging pattern has also been observed [74, 75] but attributed to the (1 1 0) reflection of sodium clusters [74], thereby supporting the proposed pore-filling mechanism. However, no diffraction patterns corresponding to sodium nano-clusters were observed in the cross-validated *in situ* ND data (Supplementary Fig. S13e). The pore size reduction observed during sodiation process via small-angle scattering, previously interpreted as the pore filled by sodium clusters [74], can instead be explained by sodium adsorption within graphene phase that occupies a portion of the pore volume.

Supplementary Figures

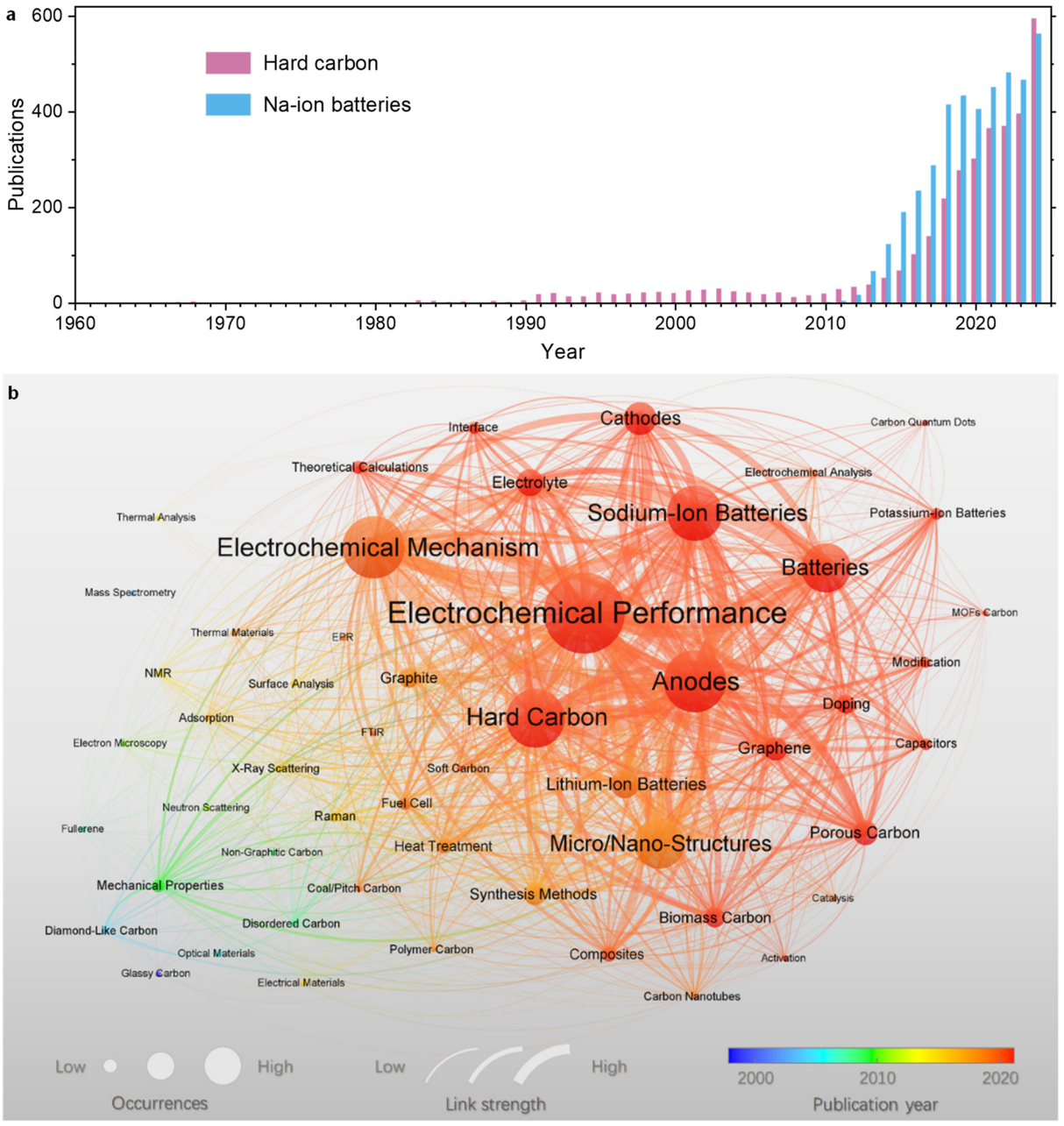

Fig. S1 | Research interest in hard carbon from 1961 to 2024. **a,** Number of research articles published on the topic of hard carbon and SIBs. **b,** Hotspot analysis for the research topic of hard carbon.

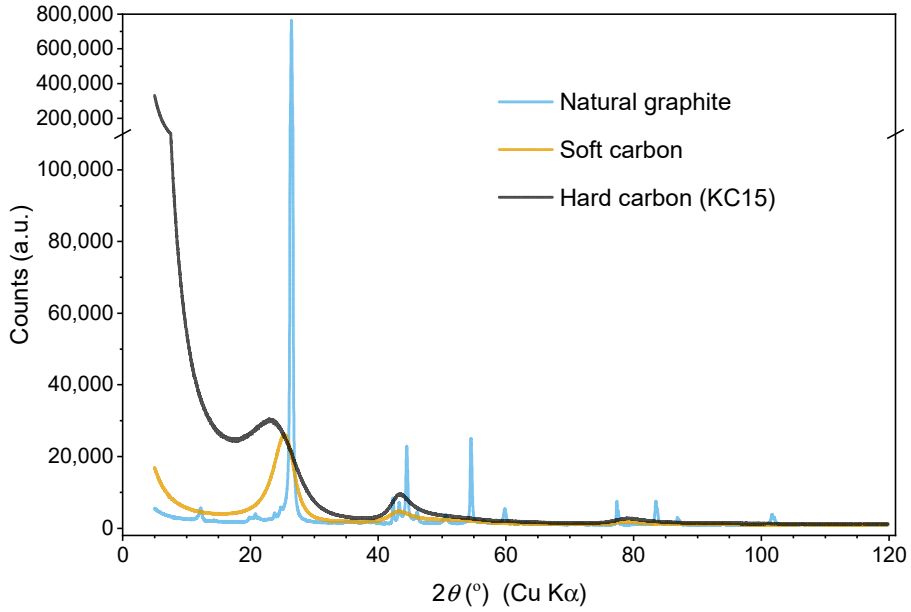

Fig. S2 | XRD patterns of natural graphite, soft carbon, and hard carbon collected on the same instrument (SmartLab, Rikagu) under identical instrumental parameters.

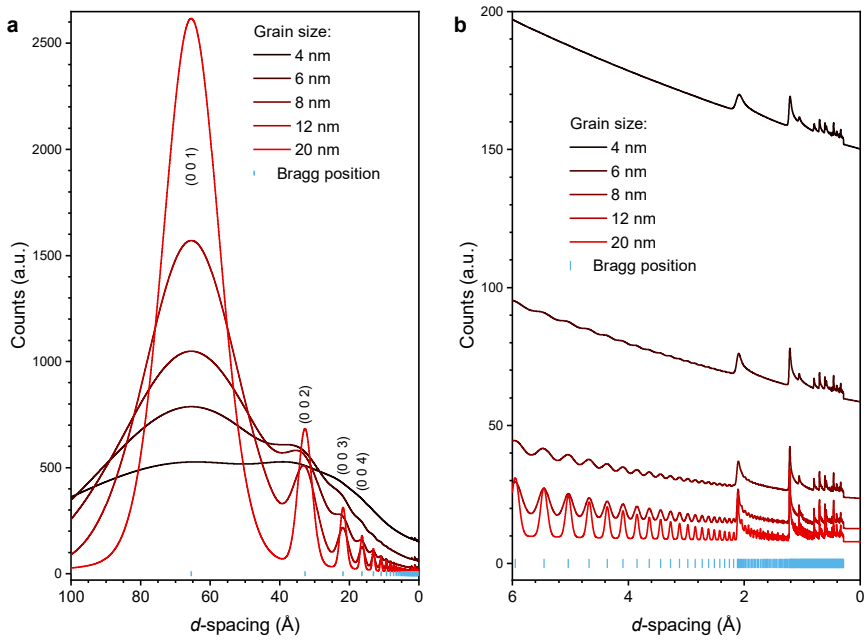

Fig. S3 | Simulated TOF-ND patterns for the graphene phase with varying grain sizes. The patterns are shown in **a,** full zoom and **b,** localized zoom.

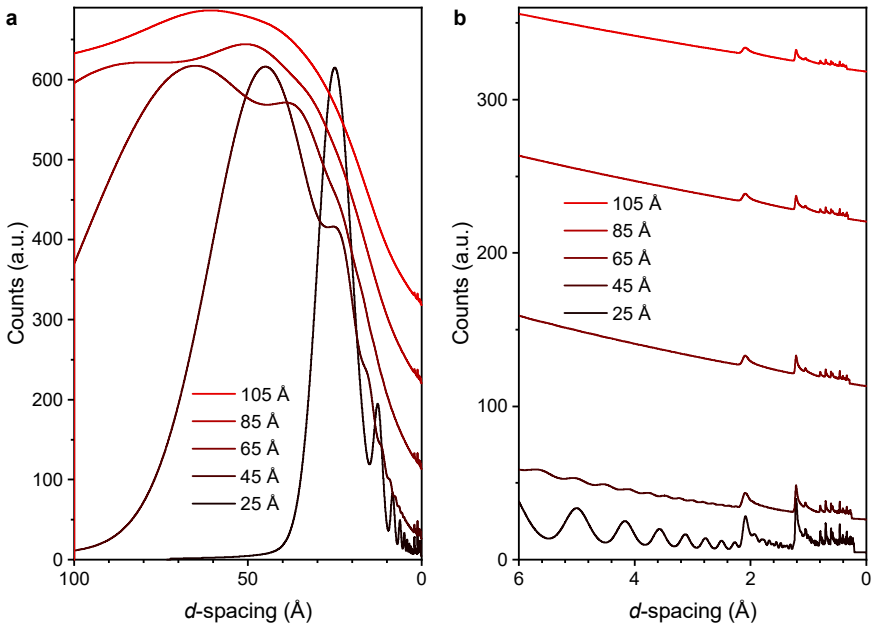

Fig. S4 | Simulated TOF-ND patterns for the graphene phase with varying lengths of *c*-axis. The patterns are shown in **a,** full zoom and **b,** localized zoom.

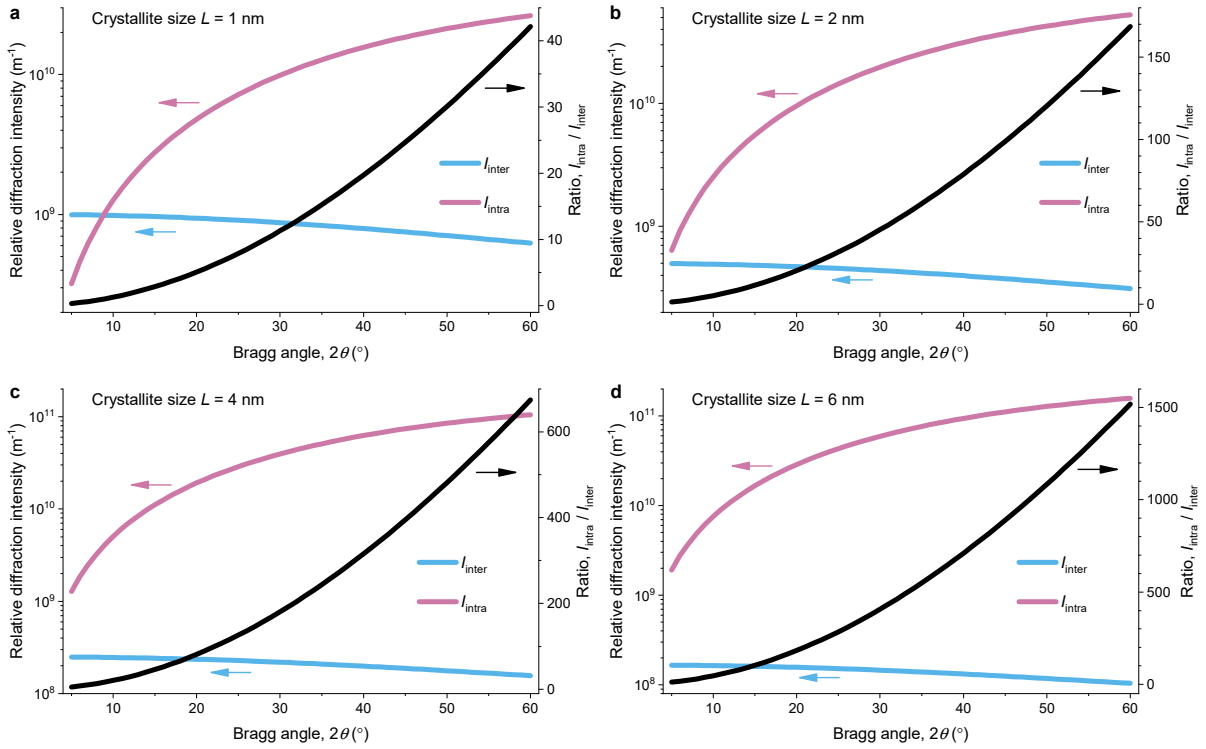

Fig. S5 | XRD contributions from the Bragg order of intra- and inter-crystallite as a function of Bragg angle for various crystallite sizes: **a,** 1 nm; **b,** 2 nm; **c,** 4nm; and **d,** 6nm.

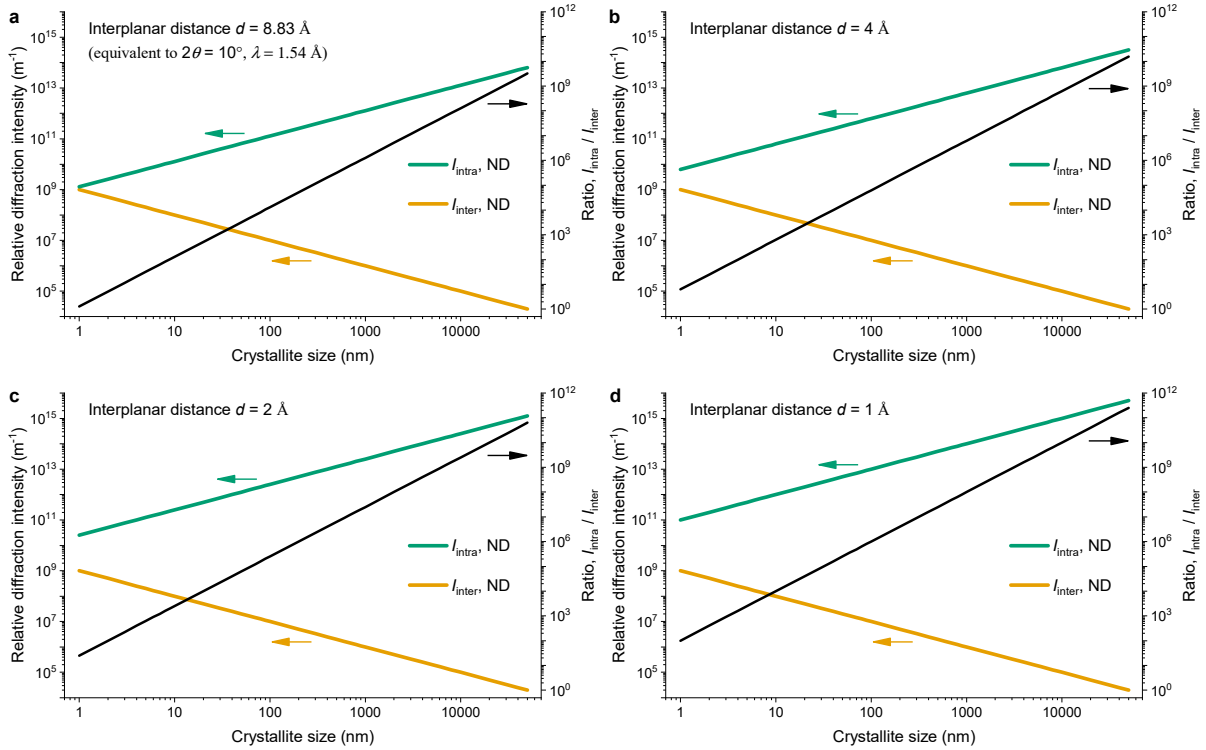

Fig. S6 | ND contributions from the Bragg order of intra- and inter-crystallite as a function of crystallite size for various interplanar distances: **a,** 8.83 Å (equivalent to the condition in Fig. 2b), **b,** 4 Å, **c,** 2 Å, and **d,** 1 Å.

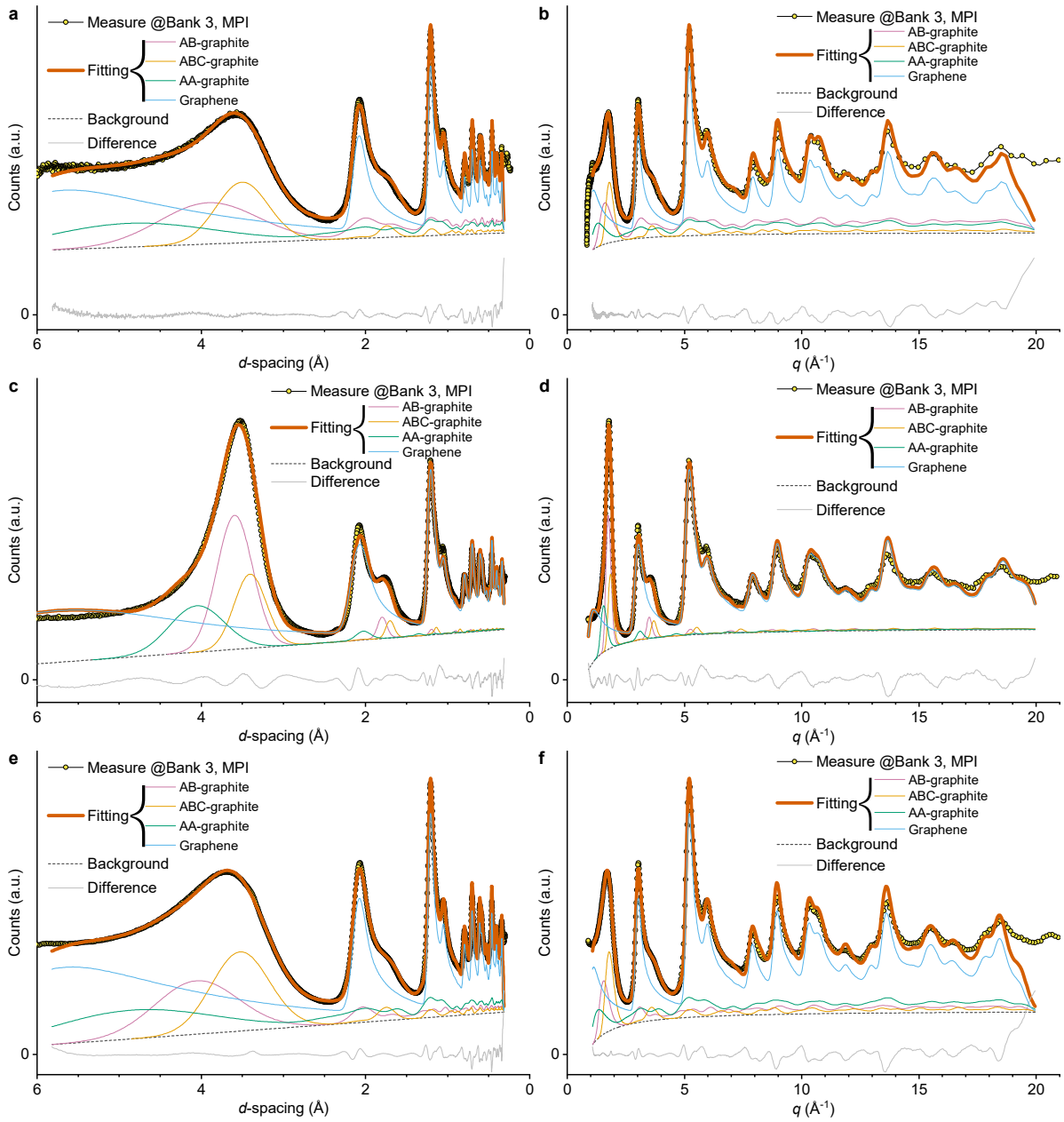

Fig. S7 | Rietveld refinements of ND data of various disordered carbon samples. **a,** Ketjenblack EC-600JD, **b,** conductive carbon black Super P, and **c,** hard carbon BSHC-350 for SIB's anode.

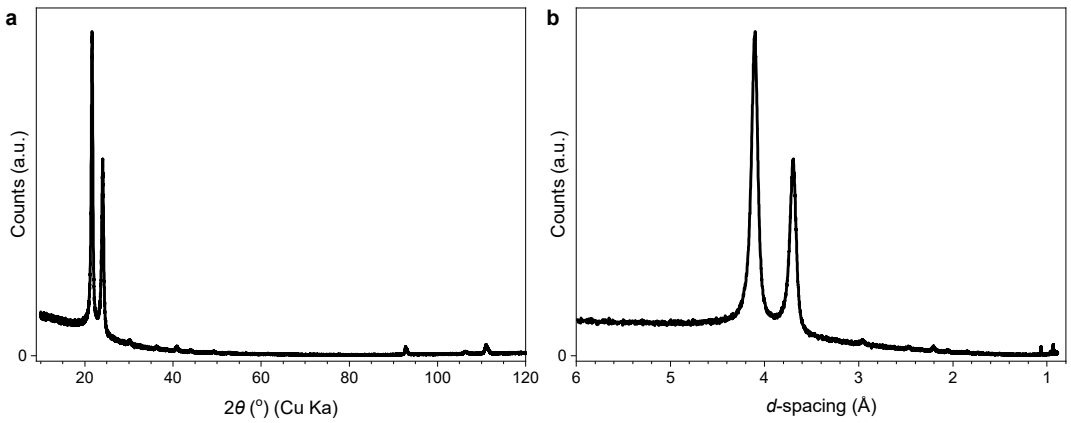

Fig. S8 | XRD patterns of the PE separator used in the in situ ND experiment, shown in **a,** 2θ and **b,** *d*-spacing.

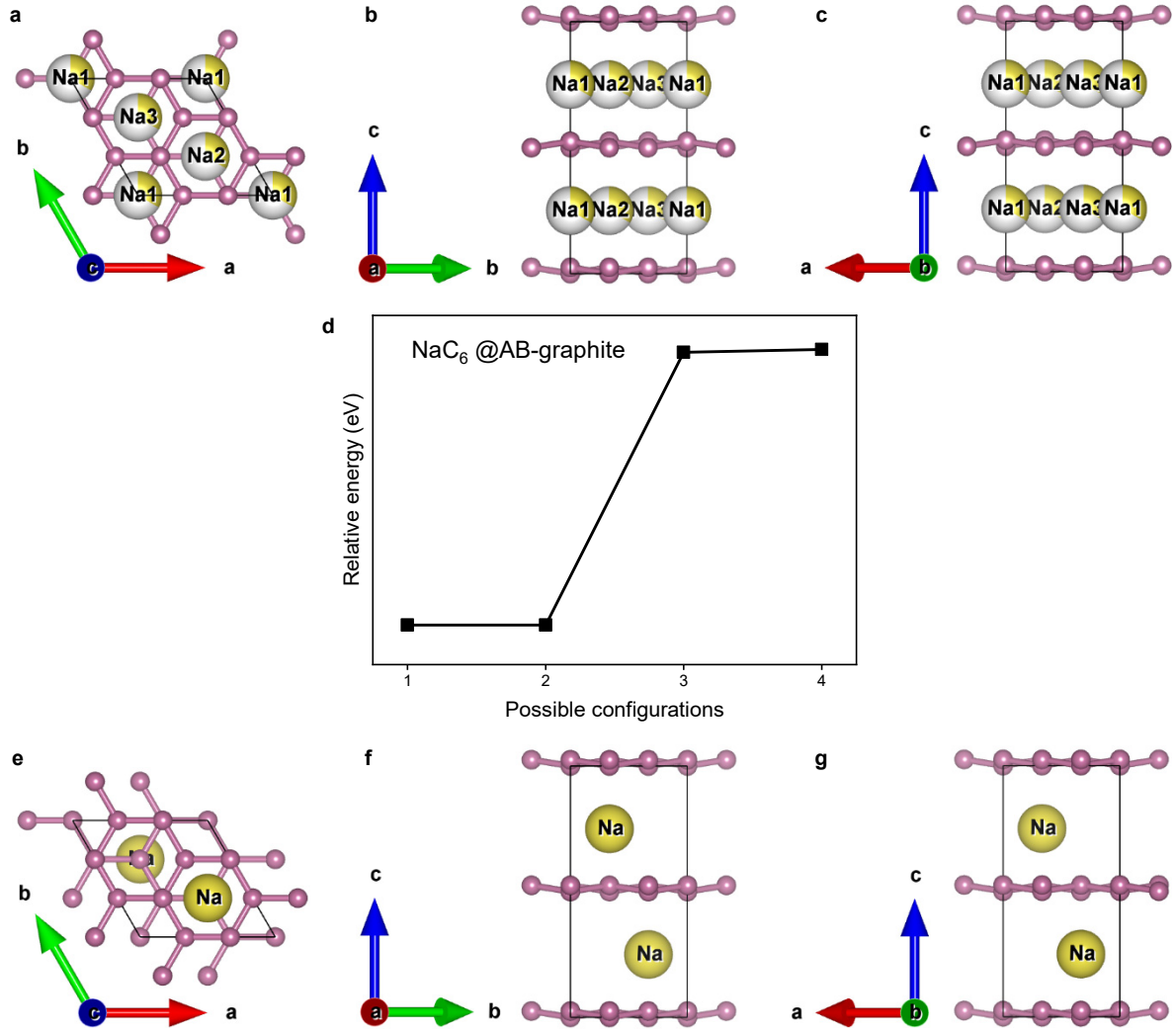

Fig. S9 | Predicted structure of fully sodiated AB-graphite, NaC_6. Average atom model used for calculations is shown along the **a,** *c*-axis, **b,** *a*-axis, and **c,** *b*-axis. **d,** Calculated results of all mathematically possible real atom configurations and their relative energies. The real atom model with the lowest energy is shown along the **e,** *c*-axis, **f,** *a*-axis, and **g,** *b*-axis.

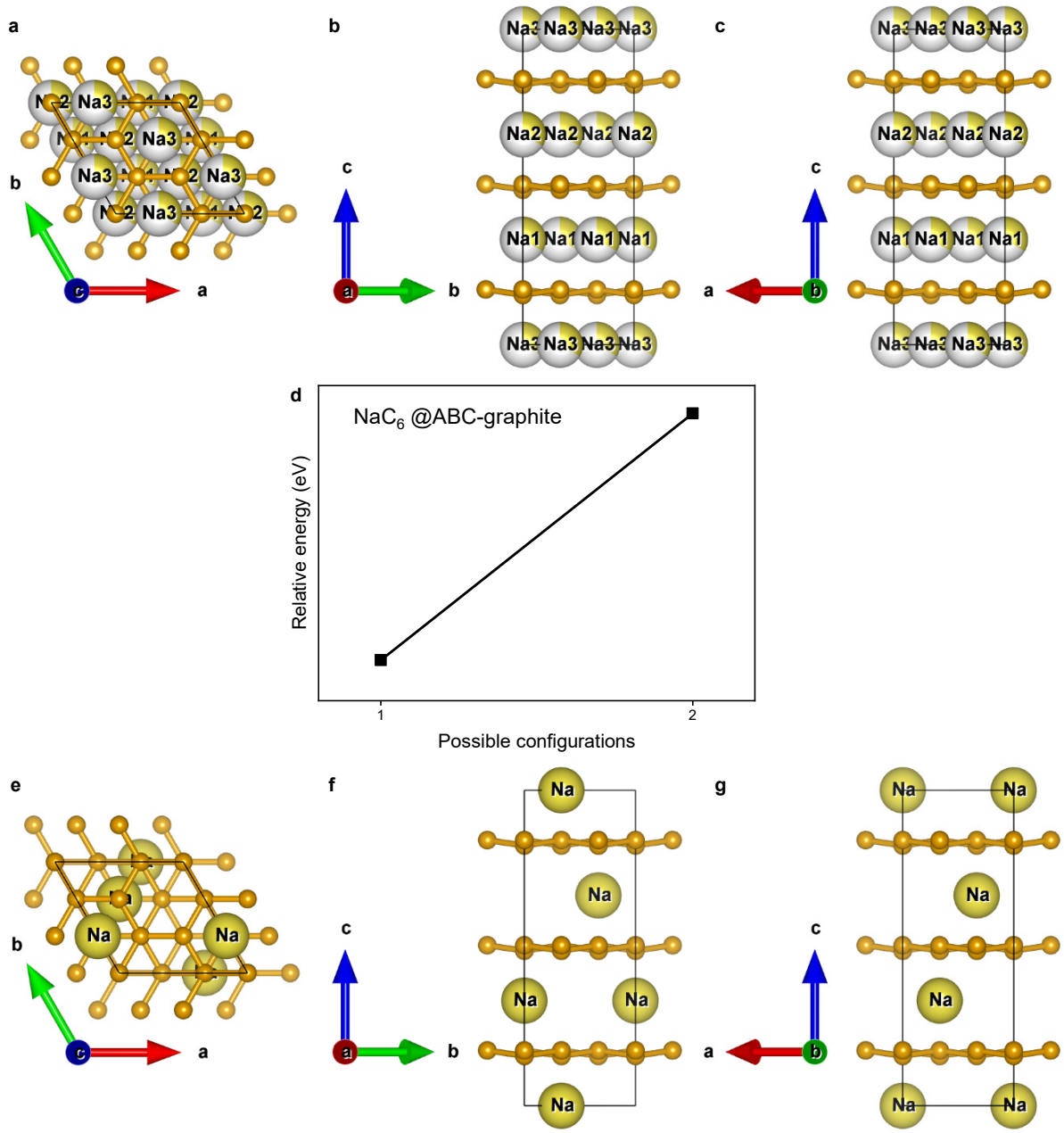

Fig. S10 | Predicted structure of fully sodiated ABC-graphite, NaC_6. Average atom model used for calculations is shown along the **a,** *c*-axis, **b,** *a*-axis, and **c,** *b*-axis. **d,** Calculated results of all mathematically possible real atom configurations and their relative energies. The real atom model with the lowest energy is shown along the **e,** *c*-axis, **f,** *a*-axis, and **g,** *b*-axis.

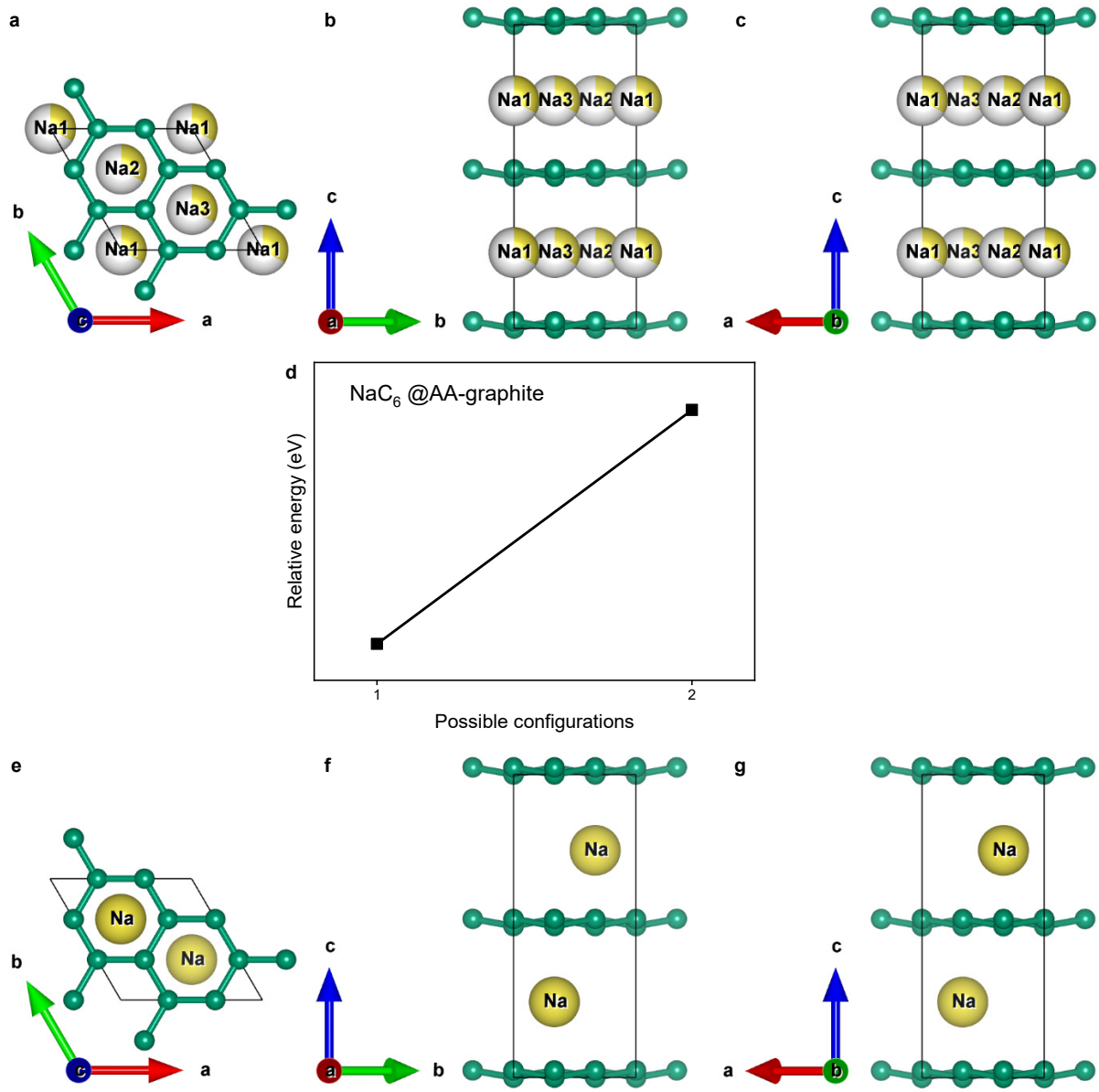

Fig. S11 | Predicted structure of fully sodiated AA-graphite, NaC_6. Average atom model used for calculations is shown along the **a,** *c*-axis, **b,** *a*-axis, and **c,** *b*-axis. **d,** Calculated results of all mathematically possible real atom configurations and their relative energies. The real atom model with the lowest energy is shown along the **e,** *c*-axis, **f,** *a*-axis, and **g,** *b*-axis.

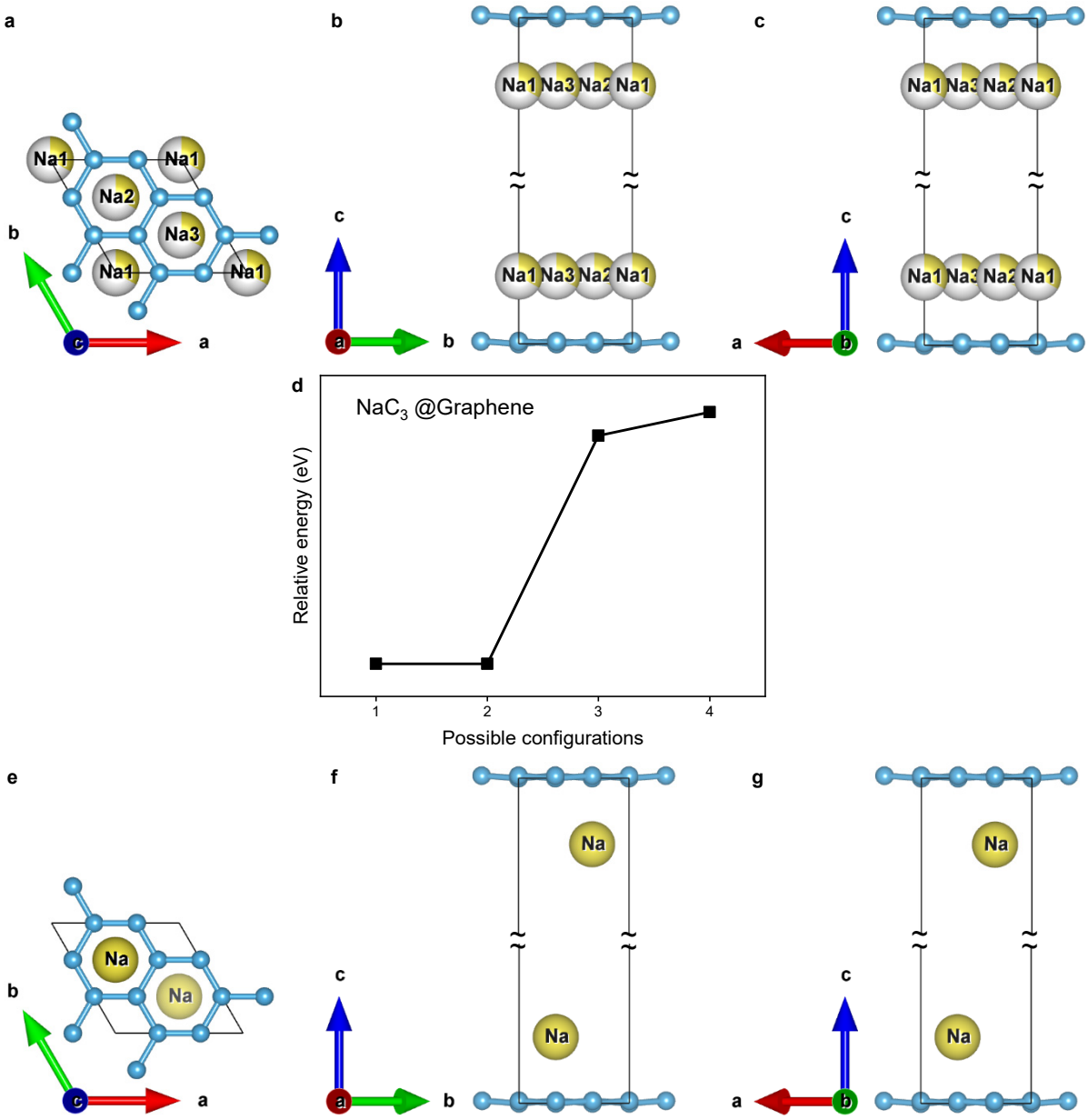

Fig. S12 | Predicted structure of fully sodiated graphene, NaC_3. Average atom model used for calculations is shown along the **a,** *c*-axis, **b,** *a*-axis, and **c,** *b*-axis. **d,** Calculated results of all mathematically possible real atom configurations and their relative energies. The real atom model with the lowest energy is shown along the **e,** *c*-axis, **f,** *a*-axis, and **g,** *b*-axis.

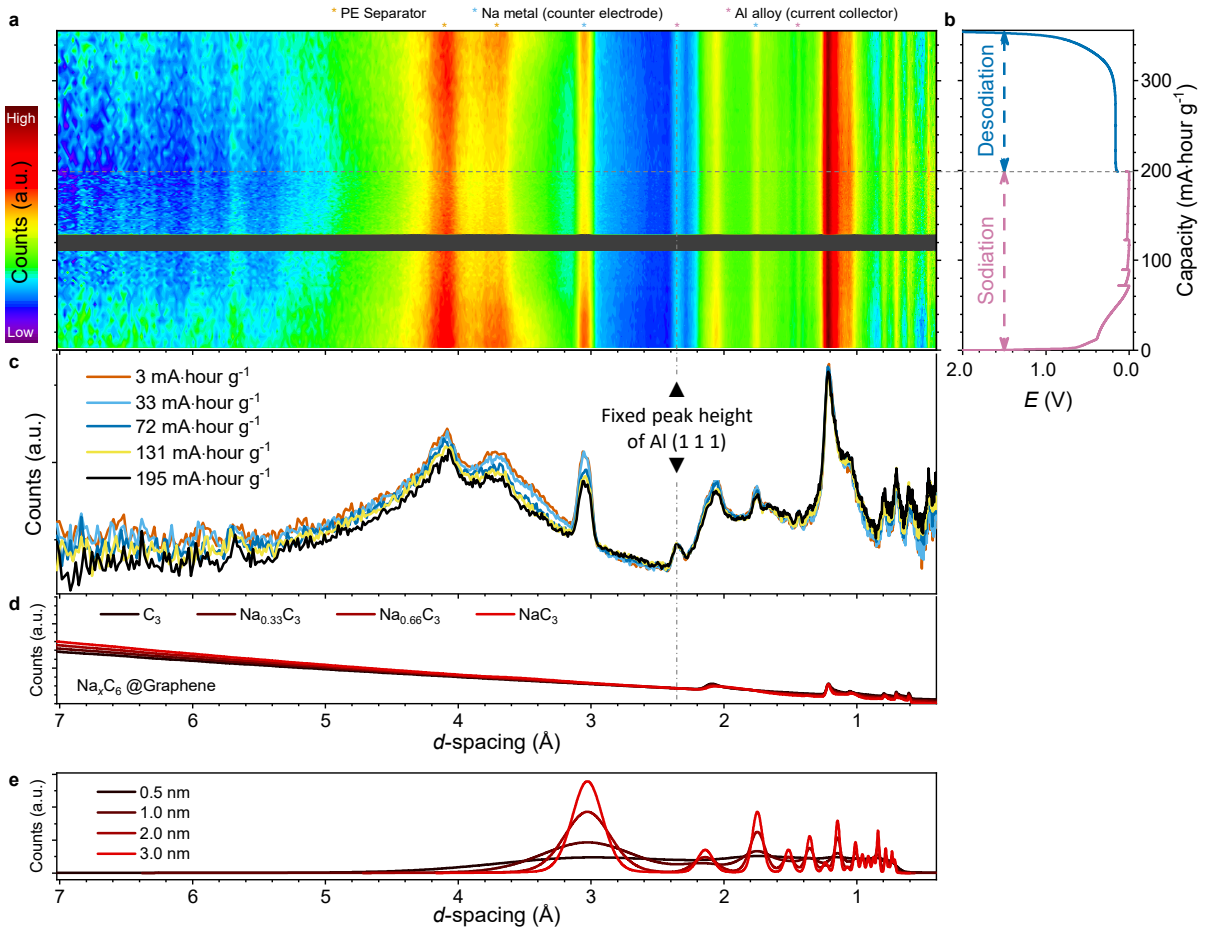

Fig. S13 | Offset patterns from the *in situ* TOF-ND (Fig. 3) for clearer observation. **a,** the ND patterns were offset to a fix intensity at the peak position of Al (1 1 1), along with **b,** simultaneous electrochemical test plot and **c,** selected ND patterns from (**a**) presented as counts versus *d*-spacing plots for clearer reference. **d,** Simulated TOF-ND patterns of sodiated graphene with the same offset at the peak position of Al (1 1 1). **e,** Simulated TOF-ND patterns of Na metal with varying grain sizes for reference.

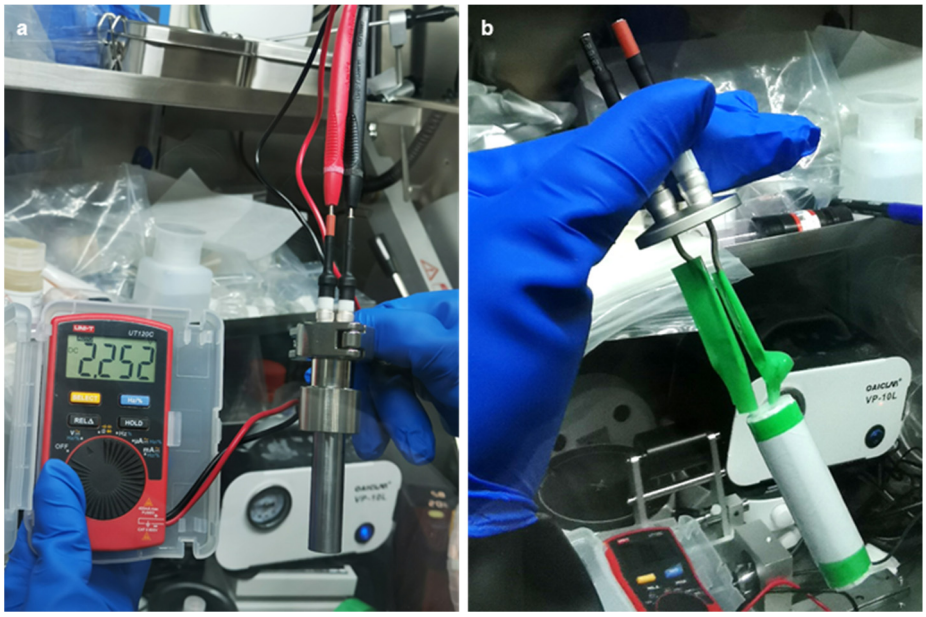

Fig. S14 | Photographs of the in situ ND cell. **a,** Full assembled state during open circuit voltage testing. **b,** Winded electrodes and separator prior to assembly.

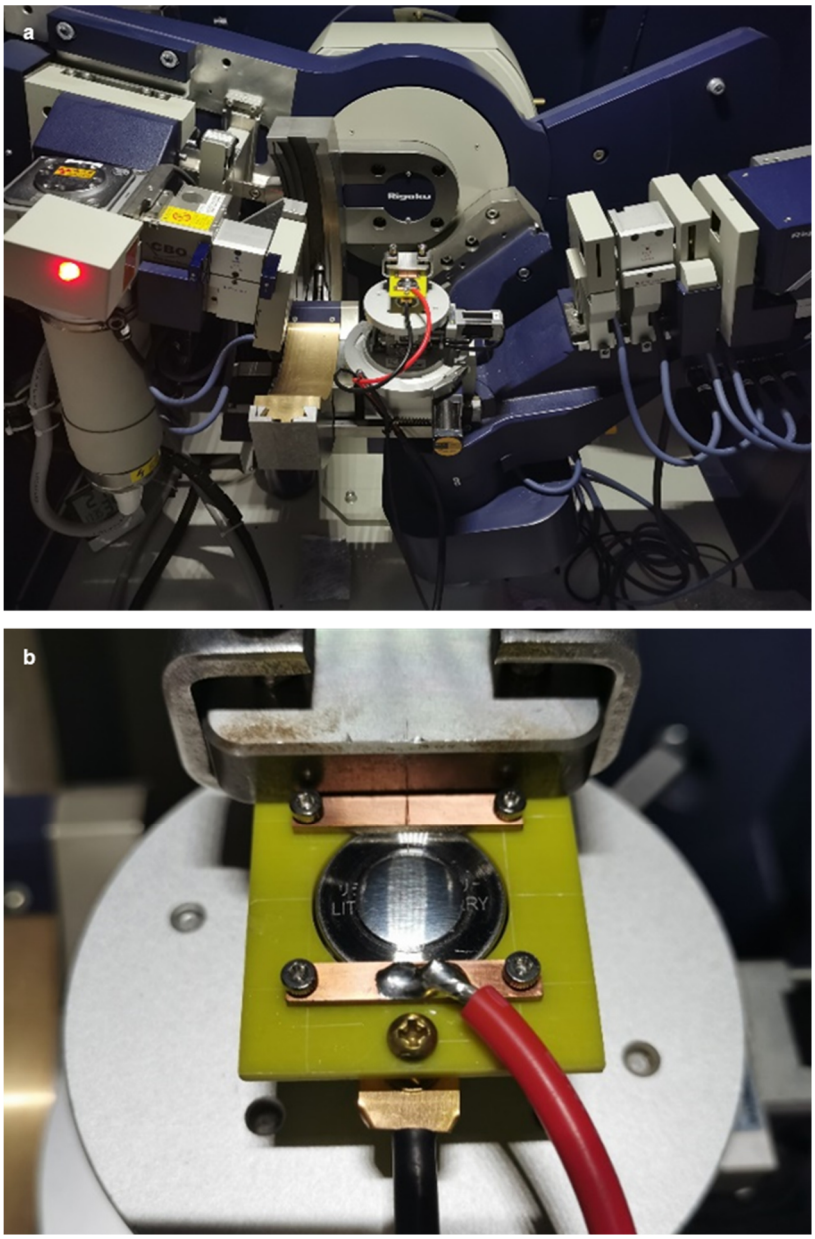

Fig. S15 | Photographs from the in situ XRD experiment. **a,** Testing state on the instrument. **b,** The in situ cell on its holder.

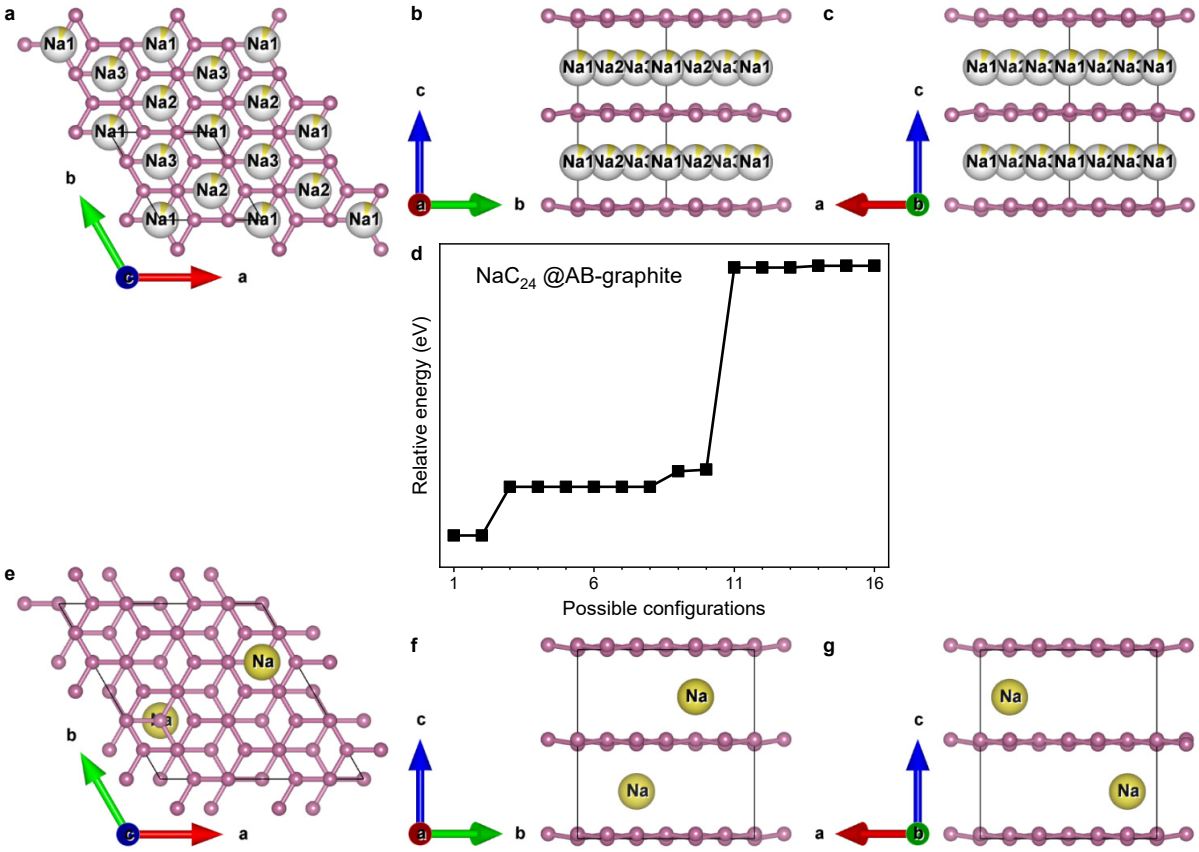

Fig. S16 | Predicted structure of partially sodiated AB-graphite, NaC_{24}. Average atom model used for calculations is shown along the **a,** *c*-axis, **b,** *a*-axis, and **c,** *b*-axis. **d,** Calculated results of all mathematically possible real atom configurations and their relative energies. The real atom model with the lowest energy is shown along the **e,** *c*-axis, **f,** *a*-axis, and **g,** *b*-axis.

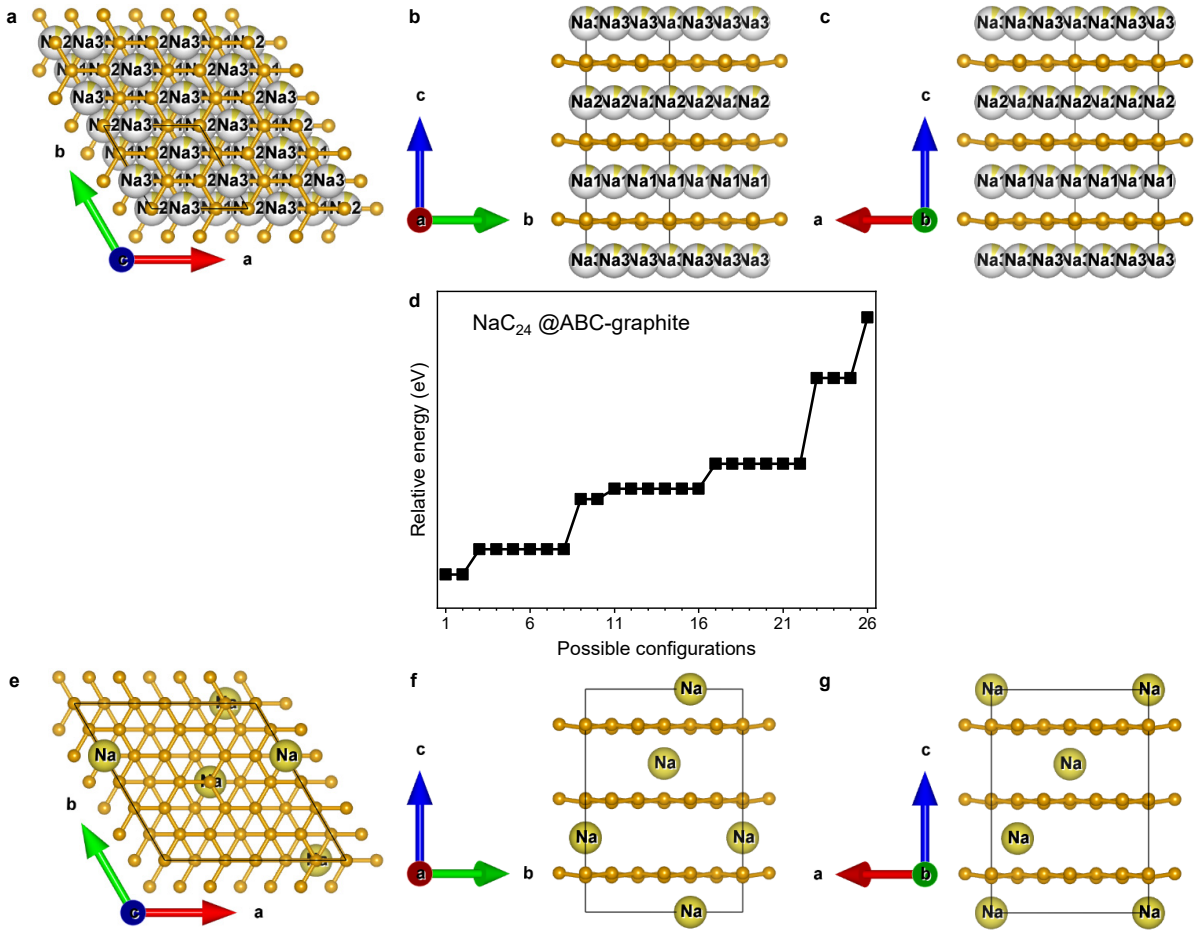

Fig. S17 | Predicted structure of partially sodiated ABC-graphite, NaC_{24}. Average atom model used for calculations is shown along the **a,** *c*-axis, **b,** *a*-axis, and **c,** *b*-axis. **d,** Calculated results of all mathematically possible real atom configurations and their relative energies. The real atom model with the lowest energy is shown along the **e,** *c*-axis, **f,** *a*-axis, and **g,** *b*-axis.

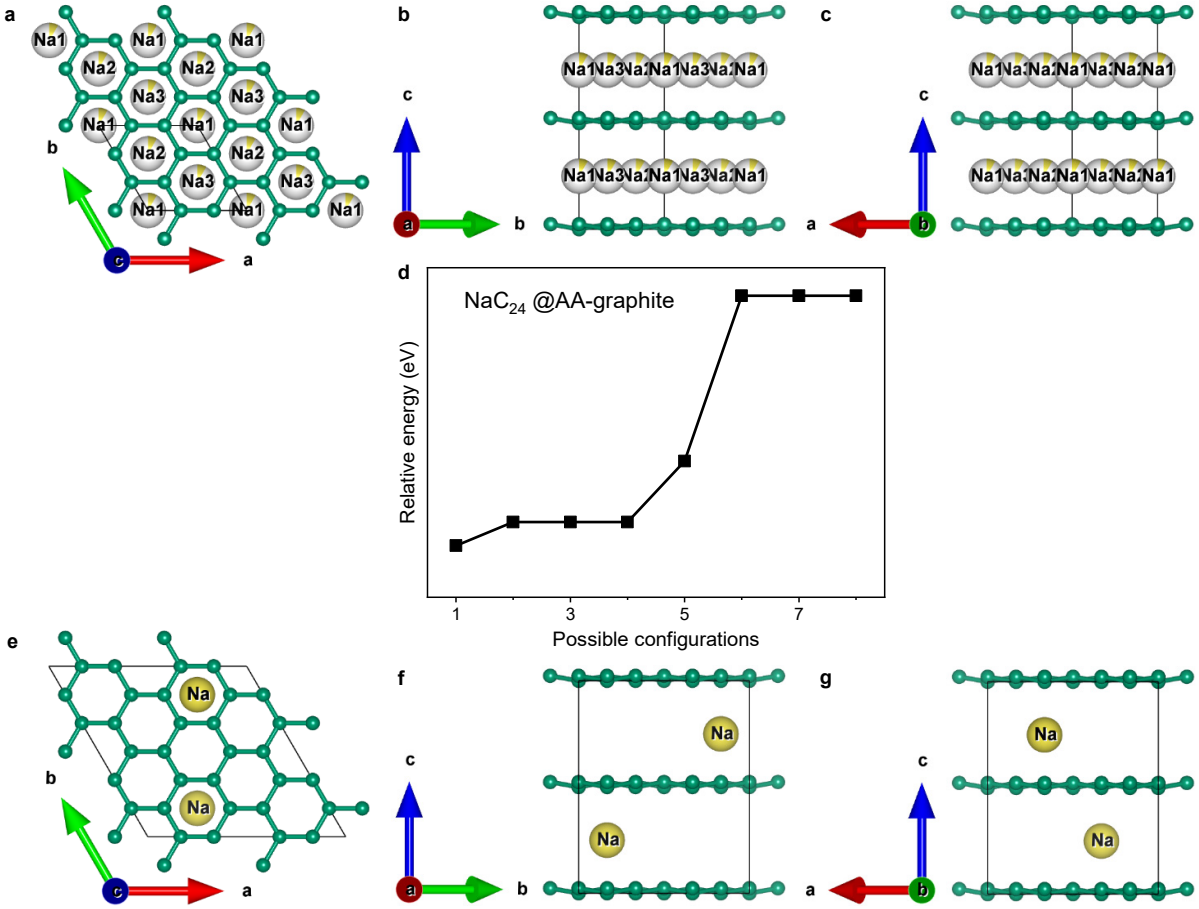

Fig. S18 | Predicted structure of partially sodiated AA-graphite, NaC_{24}. Average atom model used for calculations is shown along the **a,** *c*-axis, **b,** *a*-axis, and **c,** *b*-axis. **d,** Calculated results of all mathematically possible real atom configurations and their relative energies. The real atom model with the lowest energy is shown along the **e,** *c*-axis, **f,** *a*-axis, and **g,** *b*-axis.

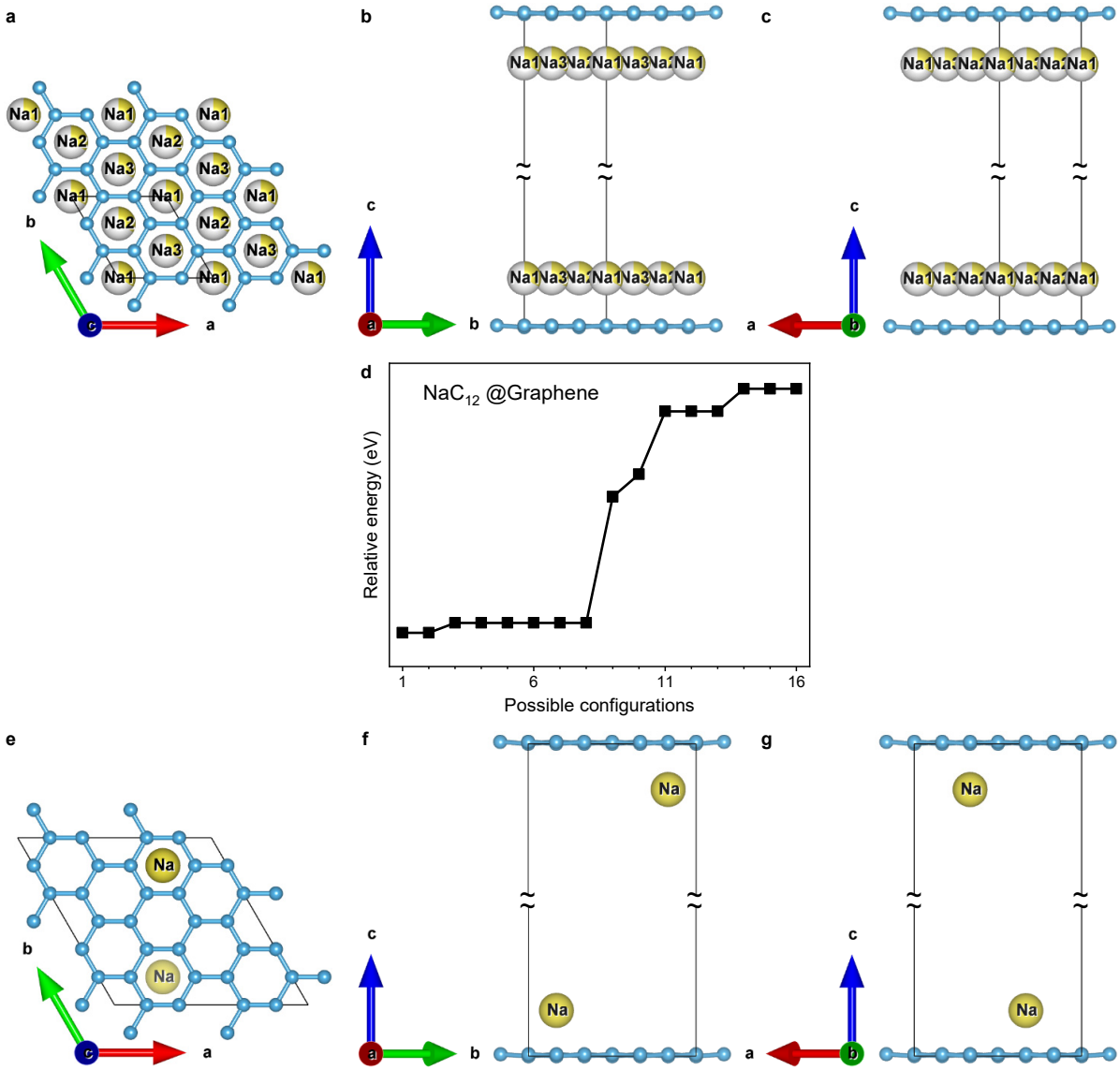

Fig. S19 | Predicted structure of partially sodiated graphene, NaC_{12}. Average atom model used for calculations is shown along the **a,** *c*-axis, **b,** *a*-axis, and **c,** *b*-axis. **d,** Calculated results of all mathematically possible real atom configurations and their relative energies. The real atom model with the lowest energy is shown along the **e,** *c*-axis, **f,** *a*-axis, and **g,** *b*-axis.

Supplementary Tables

Table S1 | Error values of the neutron/X-ray combined Rietveld refinement for the diffraction data of KC15.

Dataset	R_{exp} (%)	R_{wp} (%)	R_p (%)
Bank 2, MPI, CSNS	0.20	4.76	4.20
Bank 3, MPI, CSNS	0.10	4.61	3.67
Bank 7, MPI, CSNS	0.16	5.44	5.94
NOVA, JAPAR	0.02	4.18	3.22
Echidna, ANSTO	3.15	12.54	9.83
ID31, ESRF	1.46	13.42	9.21
SmartLab, Rikagu	1.54	6.02	3.80
Combined	0.07	4.23	4.91

Table S2 | Structural parameters of KC15 obtained from the neutron/X-ray combined Rietveld refinement.

Phase	Space group	*a* (Å)	*b* (Å)	*c* (Å)	alpha (°)	beta (°)	gamma (°)	Atom	Wyckoff position	*x*	*y*	*z*	Occupancy
AB-graphite	$P6_3mc$ (186)	2.4429(2)	2.4429(2)	7.889(7)	90	90	120	C_1	2*a*	0	0	0	1
								C_2	2*b*	0.333333	0.666667	0.0596(11)	1
ABC-graphite	*R*-3*m*:*R* (166)	3.756(2)	3.756(2)	3.756(2)	37.95(2)	37.95(2)	37.95(2)	C	2*c*	0.1560(4)	0.1560(4)	0.1560(4)	1
AA-graphite	*P*3 (143)	2.4429(2)	2.4429(2)	4.574(5)	90	90	120	C_1	1*b*	0.333333	0.666667	0.0475(16)	1
								C_2	1*c*	0.666667	0.333333	0	1
Graphene	*P*3 (143)	2.4429(2)	2.4429(2)	65.46(4)	90	90	120	C_1	1*b*	0.333333	0.666667	0.0013(2)	1
								C_2	1*c*	0.666667	0.333333	0	1

Table S3 | Phase proportion and additional structural information of KC15 obtained or derived from the neutron/X-ray combined Rietveld refinement results.

Phase	Content* (wt.%)	Grain size* (nm)	Prefer orrientation & coefficient*	L_a (nm)	L_c (nm)	Height of chair conformation (Å)	Interlayer distance (Å)
AB-graphite	10.74(26)	1.538(10)	(002), 0.718(6)	1.538(10)	1.104(16)	0.470(9)	3.945(3)
ABC-graphite	10.94(40)	1.604(5)	(111), 0.518(8)	1.604(5)	0.831(15)	0.223(9)	3.481(2)
AA-graphite	23.63(24)	1.023(6)	(001), 1.096(4)	1.023(6)	1.121(11)	0.217(8)	4.574(5)
Graphene	54.69(36)	4.716(17)	(001), 1.156(2)	4.716(17)	-	0.085(13)	65.46(4)

*: Directly refined parameters; other unmarked parameters were derived from direct parameters.

Table S4 | Error values of the neutron/X-ray combined refinement for the PDF data of KC15.

Dataset	R_{wp} (%)	R_p (%)
MPI, CSNS	24.71	21.69
NOVA, JAPAR	27.67	24.07
ID31, ESRF	27.46	25.44
P02.1, DESY	36.89	37.19
Combined	26.16	23.68

Table S5 | Structural parameters obtained from the neutron/X-ray combined refinement for the PDF data of KC15.

Phase	Space group	*a* (Å)	*b* (Å)	*c* (Å)	alpha (°)	beta (°)	gamma (°)	Atom	Wyckoff position	*x*	*y*	*z*	Occupancy
AB-graphite	$P6_3mc$ (186)	2.4595(6)	2.4595(6)	8.10(3)	90	90	120	C_1	2a	0	0	0	1
								C_2	2b	0.33333	0.66667	0.039(2)	1
ABC-graphite	R-3m:R (166)	3.730(4)	3.730(4)	3.730(4)	38.50(4)	38.50(4)	38.50(4)	C	2c	0.1581(2)	0.1581(2)	0.1581(2)	1
AA-graphite	P3 (143)	2.4595(6)	2.4595(6)	4.164(5)	90	90	120	C_1	2b	0.33333	0.66667	0.021(3)	1
								C_2	2b	0.66667	0.33333	0	1
Graphene	P3 (143)	2.4595(6)	2.4595(6)	65	90	90	120	C_1	2b	0.33333	0.66667	0.005(72)	1
								C_2	2b	0.66667	0.33333	0	1

Table S6 | Rietveld refinement results of disordered carbon samples using the structural framework of the four phases.

Sample	R_{wp} (%)	R_p (%)	Phase	Content (wt.%)	Grain size (nm)	*a* (Å)	*b* (Å)	*c* (Å)	alpha (°)	beta (°)	gamma (°)
EC-600JD	3.51	2.80	AB-graphite	18.4 (1.8)	1.08 (2)	2.449 (1)	2.449 (1)	7.83 (5)	90	90	120
			ABC-graphite	10.4 (1.5)	1.65 (2)	3.779 (4)	3.779 (4)	3.779 (4)	37.81 (4)	37.81 (4)	37.81 (4)
			AA-graphite	11.6 (1.0)	1.00 (5)	2.449 (1)	2.449 (1)	4.88 (3)	90	90	120
			Graphene	59.6 (1.7)	3.21 (3)	2.449 (1)	2.449 (1)	62.3 (6)	90	90	120
Super P	6.96	6.56	AB-graphite	1.8 (2)	2.56 (7)	2.459 (2)	2.459 (2)	7.20 (2)	90	90	120
			ABC-graphite	5.3 (8)	2.57 (6)	3.69 (1)	3.69 (1)	3.694 (11)	38.88 (12)	38.88 (12)	38.88 (12)
			AA-graphite	1.1 (1)	2.11 (9)	2.459 (2)	2.459 (2)	4.06 (3)	90	90	120
			Graphene	91.8 (8)	2.21 (3)	2.459 (2)	2.459 (2)	53.6 (3)	90	90	120
BSHC-350	2.93	3.89	AB-graphite	8.2 (1.5)	1.27 (2)	2.444 (1)	2.444 (1)	8.12 (4)	90	90	120
			ABC-graphite	12.5 (1.4)	1.72 (3)	3.797 (6)	3.797 (6)	3.797 (6)	37.54 (6)	37.54 (6)	37.54 (6)
			AA-graphite	12.7 (1.0)	1.00 (6)	2.444 (1)	2.444 (1)	4.85 (3)	90	90	120
			Graphene	66.7 (1.7)	3.38 (4)	2.444 (1)	2.444 (1)	62.9 (5)	90	90	120

Table S7 | Supercells of the sodiated phases derived from the original unit cells of the four phases of KC15.

Phase	Chemical formular of original unit cell	Insertion sites for Na atom	Chemical formular of targeted unit cell	Expansion ratio of supercell	Sizes of supercell
AB-graphite	C_4	2	Na_2C_{12}	3	$\sqrt{3}\times\sqrt{3}\times1$
ABC-graphite	C_2	3	Na_3C_{18}	9	$\sqrt{3}\times\sqrt{3}\times3$
AA-graphite	C_2	1	NaC_6	3	$\sqrt{3}\times\sqrt{3}\times1$
Graphene	C_2	2	Na_2C_6	3	$\sqrt{3}\times\sqrt{3}\times1$

References

50. Saurel D, Segalini J, Jauregui M, Pendashteh A, Daffos B, Simon P*, et al.* A SAXS outlook on disordered carbonaceous materials for electrochemical energy storage. *Energy Storage Mater* 2019, **21:** 162-173.
51. Cançado LG, Takai K, Enoki T, Endo M, Kim YA, Mizusaki H*, et al.* General equation for the determination of the crystallite size La of nanographite by Raman spectroscopy. *Appl Phys Lett* 2006, **88**(16)**:** 163106.
52. Xu J, Xia Y, Li Z, Chen H, Wang X, Sun Z*, et al.* Multi-physics instrument: Total scattering neutron time-of-flight diffractometer at China Spallation Neutron Source. *Nuclear Instruments and Methods in Physics Research Section A: Accelerators, Spectrometers, Detectors and Associated Equipment* 2021, **1013:** 165642.
53. Nakajima K, Kawakita Y, Itoh S, Abe J, Aizawa K, Aoki H*, et al.* Materials and Life Science Experimental Facility (MLF) at the Japan Proton Accelerator Research Complex II: Neutron Scattering Instruments. *Quantum Beam Science*; 2017.
54. Avdeev M, Hester JR. ECHIDNA: a decade of high-resolution neutron powder diffraction at OPAL. *J Appl Crystallogr* 2018, **51**(6)**:** 1597-1604.
55. Ashiotis G, Deschildre A, Nawaz Z, Wright JP, Karkoulis D, Picca FE*, et al.* The fast azimuthal integration Python library: pyFAI. *J Appl Crystallogr* 2015, **48**(2)**:** 510-519.
56. Kieffer J, Valls V, Blanc N, Hennig C. New tools for calibrating diffraction setups. *Journal of Synchrotron Radiation* 2020, **27**(2)**:** 558-566.
57. Juhas P, Davis T, Farrow CL, Billinge SJL. PDFgetX3: a rapid and highly automatable program for processing powder diffraction data into total scattering pair distribution functions. *J Appl Crystallogr* 2013, **46**(2)**:** 560-566.
58. Yang X, Juhás P, Farrow CL, Billinge SJL. xPDFsuite: an end-to-end software solution for high throughput pair distribution function transformation, visualization and analysis. 2015.
59. Momma K, Izumi F. VESTA 3 for three-dimensional visualization of crystal, volumetric and morphology data. *J Appl Crystallogr* 2011, **44**(6)**:** 1272-1276.
60. Okhotnikov K, Charpentier T, Cadars S. Supercell program: a combinatorial structure-generation approach for the local-level modeling of atomic substitutions and partial occupancies in crystals. *Journal of Cheminformatics* 2016, **8**(1)**:** 17.
61. Kresse G, Furthmüller J. Efficient iterative schemes for ab initio total-energy calculations using a plane-wave basis set. *Physical Review B* 1996, **54**(16)**:** 11169-11186.
62. Kohn W, Sham LJ. Self-Consistent Equations Including Exchange and Correlation Effects. *Phys Rev* 1965, **140**(4A)**:** A1133-A1138.
63. Blöchl PE. Projector augmented-wave method. *Physical Review B* 1994, **50**(24)**:** 17953-17979.
64. Perdew JP, Burke K, Ernzerhof M. Generalized Gradient Approximation Made Simple. *Phys Rev Lett* 1996, **77**(18)**:** 3865-3868.
65. van Eck NJ, Waltman L. Software survey: VOSviewer, a computer program for bibliometric mapping. *Scientometrics* 2010, **84**(2)**:** 523-538.
66. Rosenberg RA, Love PJ, Rehn V. Polarization-dependent C(K) near-edge x-ray-absorption fine structure of graphite. *Physical Review B* 1986, **33**(6)**:** 4034-4037.
67. Fischer DA, Wentzcovitch RM, Carr RG, Continenza A, Freeman AJ. Graphitic interlayer states: A carbon K near-edge x-ray-absorption fine-structure study. *Physical Review B* 1991, **44**(3)**:** 1427-1429.
68. Lee V, Whittaker L, Jaye C, Baroudi KM, Fischer DA, Banerjee S. Large-Area Chemically Modified Graphene Films: Electrophoretic Deposition and Characterization by Soft X-ray Absorption Spectroscopy. *Chem Mater* 2009, **21**(16)**:** 3905-3916.
69. Xu J, Krüger P, Natoli CR, Hayakawa K, Wu Z, Hatada K. X-ray absorption spectra of graphene and graphene oxide by full-potential multiple scattering calculations with self-consistent charge density. *Physical Review B* 2015, **92**(12)**:** 125408.
70. Kaznacheyev K, Osanna A, Jacobsen C, Plashkevych O, Vahtras O, Ågren*, et al.* Innershell Absorption Spectroscopy of Amino Acids. *The Journal of Physical Chemistry A* 2002, **106**(13)**:** 3153-3168.
71. Jeong HK, Noh HJ, Kim JY, Jin MH, Park CY, Lee YH. X-ray absorption spectroscopy of graphite oxide. *Europhys Lett* 2008, **82**(6)**:** 67004.

72. Sun F, Wang H, Qu Z, Wang K, Wang L, Gao J*, et al.* Carboxyl-Dominant Oxygen Rich Carbon for Improved Sodium Ion Storage: Synergistic Enhancement of Adsorption and Intercalation Mechanisms. *Adv Energy Mater* 2021, **11**(1)**:** 2002981.
73. Zhuang H-k, Li W-c, He B, Lv J-h, Wang J-s, Shen M-y*, et al.* Increasing the interlayer spacing and generating closed pores to produce petroleum coke-based carbon materials for sodium ion storage. *New Carbon Materials* 2024, **39**(3)**:** 549-560.
74. Morikawa Y, Nishimura S-i, Hashimoto R-i, Ohnuma M, Yamada A. Mechanism of Sodium Storage in Hard Carbon: An X-Ray Scattering Analysis. *Adv Energy Mater* 2020, **10**(3)**:** 1903176.
75. Mathiesen JK, Väli R, Härmas M, Lust E, Fold von Bülow J, Jensen KMØ*, et al.* Following the in-plane disorder of sodiated hard carbon through operando total scattering. *J Mater Chem A* 2019, **7**(19)**:** 11709-11717.